INSIGHTS GAINED THROUGH IMAGE ANALYSIS DURING IN-SITU MICROMECHANICAL EXPERIMENTS (Preprint)

P.A. Shade and M.D. Uchic

Metals Branch
Metals, Ceramics, & NDE Division

R. Wheeler

UES Inc. and MicroTesting Solutions LLC

NOVEMBER 2011

STINFO COPY

AIR FORCE RESEARCH LABORATORY
MATERIALS AND MANUFACTURING DIRECTORATE
WRIGHT-PATTERSON AIR FORCE BASE, OH 45433-7750
AIR FORCE MATERIEL COMMAND
UNITED STATES AIR FORCE

REPORT DOCUMENTATION PAGE

1. REPORT DATE *(DD-MM-YY)*	2. REPORT TYPE	3. DATES COVERED *(From - To)*
November 2011	Journal Article Preprint	01 October 2011 – 01 October 2011

4. TITLE AND SUBTITLE	5a. CONTRACT NUMBER
INSIGHTS GAINED THROUGH IMAGE ANALYSIS DURING IN-SITU MICROMECHANICAL EXPERIMENTS (Preprint)	IN-HOUSE
	5b. GRANT NUMBER
	5c. PROGRAM ELEMENT NUMBER 62102F

6. AUTHOR(S)	5d. PROJECT NUMBER
P.A. Shade and M.D. Uchic (Metals, Ceramics, & NDE Division, Metals Branch) R. Wheeler (UES Inc. and MicroTesting Solutions LLC)	4347
	5e. TASK NUMBER 20
	5f. WORK UNIT NUMBER LM121100

7. PERFORMING ORGANIZATION NAME(S) AND ADDRESS(ES)		8. PERFORMING ORGANIZATION REPORT NUMBER
Metals, Ceramics, & NDE Division, Metals Branch (AFRL/RXLM) Air Force Research Laboratory Materials and Manufacturing Directorate Wright-Patterson Air Force Base, OH 45433-7750 Air Force Materiel Command, United States Air Force	UES Inc. ------------------ MicroTesting Solutions LLC	AFRL-RX-WP-TP-2011-4392

9. SPONSORING/MONITORING AGENCY NAME(S) AND ADDRESS(ES)	10. SPONSORING/MONITORING AGENCY ACRONYM(S)
Air Force Research Laboratory Materials and Manufacturing Directorate Wright-Patterson Air Force Base, OH 45433-7750 Air Force Materiel Command United States Air Force	AFRL/RXLM
	11. SPONSORING/MONITORING AGENCY REPORT NUMBER(S) AFRL-RX-WP-TP-2011-4392

12. DISTRIBUTION/AVAILABILITY STATEMENT
Approved for public release; distribution unlimited.

13. SUPPLEMENTARY NOTES
PAO case number 88ABW-2011-5362, cleared 11 October 2011. The U.S. Government is joint author of this work and has the right to use, modify, reproduce, release, perform, display, or disclose the work. Submitted to JOM. Document contains color.

14. ABSTRACT

A custom in-situ testing system has been developed to allow the quantitative study of deformation behavior in micro-sized specimens with compressive or tensile loading, which allows for ready control of the lateral test frame stiffness. Micromechanical tests have been conducted within the chamber of an SEM, which allows concurrent visualization of plastic flow during the mechanical test. Three distinct experiments are presented for the single crystal nickel-base superalloy René N5, each carried out under the same loading orientation on samples of similar size. Very different mechanical responses are reflected in the stress-strain curves for these experiments that can be understood by correlating specimen morphology change during plastic flow with the test boundary conditions.

15. SUBJECT TERMS
in-situ testing, microtest, microcompression, microtension, in-situ SEM

16. SECURITY CLASSIFICATION OF:			17. LIMITATION OF ABSTRACT:	18. NUMBER OF PAGES	19a. NAME OF RESPONSIBLE PERSON (Monitor)
a. REPORT Unclassified	b. ABSTRACT Unclassified	c. THIS PAGE Unclassified	SAR	22	Andrew Rosenberger
					19b. TELEPHONE NUMBER *(Include Area Code)* N/A

Insights gained through image analysis during in-situ micromechanical experiments

R. Wheeler[1, 2], P.A. Shade[3], M.D. Uchic[3]

[1]UES Inc., Dayton, OH
[2]MicroTesting Solutions LLC, Columbus, OH
[3]Air Force Research Laboratory, Materials & Manufacturing Directorate, Wright-Patterson AFB, OH

Abstract

A custom in-situ testing system has been developed to allow the quantitative study of deformation behavior in micro-sized specimens with compressive or tensile loading, which allows for ready control of the lateral test frame stiffness. Micromechanical tests have been conducted within the chamber of an SEM, which allows concurrent visualization of plastic flow during the mechanical test. Three distinct experiments are presented for the single crystal nickel-base superalloy René N5, each carried out under the same loading orientation on samples of similar size. Very different mechanical responses are reflected in the stress-strain curves for these experiments that can be understood by correlating specimen morphology change during plastic flow with the test boundary conditions.

Keywords: in-situ testing, microtest, microcompression, microtension, in-situ SEM

1. Introduction

There is a growing interest in development of techniques for mechanical testing of samples with micron-scale dimensions [1]. This is driven by studies focused on the direct application of small structures in some functioning system (e.g., MEMS, NEMS, thin films, etc.), studies to measure the local property response in a bulk material (e.g., single grain properties from a polycrystalline material), exploration of deformation micromechanisms, and studies to validate simulation tools that predict plastic deformation behavior. A number of comprehensive reviews have recently addressed the state-of-the-art in testing methodologies and their applications at the micro-scale [2-7].

The present study describes the application of a custom in-situ testing system developed to measure the plastic flow behavior in micro-scale test specimens with lateral dimensions ranging from sub-micron to tens-of-microns. This system supports both compressive and tensile loading. Microspecimens can be tested from arbitrary locations and orientations while either attached to the bulk substrate at one end or freestanding. Imaging can be carried out within the SEM at normal incidence to the loading direction or at large angles defined by the limits of the microscope stage, which provides a critical tool for interpreting deformation behavior [8]. Spatial and temporal distribution of deformation events is obtained through continuous automated recording of SEM images during testing.   Importantly, the test apparatus allows independent control of the lateral stiffness of the loading train. Test system lateral stiffness has recently been demonstrated

to have a large impact on the observed deformation behavior [9-11], and was varied in the present study to produce three distinct experiments.

2. Micromechanical Testing and Imaging Analyses

Figure 1 shows a schematic illustration of the basic components of the in-situ testing device used in the present experiments. A detailed description of the test frame can be found elsewhere [11]. The load train is equipped with a piezoelectric actuator, providing sub-nanometer displacement control over a total stroke of 40 µm. Tests are conducted under open-loop displacement-rate control. An alignment flexure is employed between the actuator and a strain-gage-based load cell to ensure axial loading. The load range and sensitivity of the system configuration used in these experiments was 100 g and 0.01 g, respectively. The compression platen or tensile grip is attached to the load cell and the sample to a micro-positioning stage.

This test frame has a very high intrinsic lateral stiffness. Further, the setup allows for an easy exchange of various compression platens and tensile grips, and the net lateral constraint imposed on the microsamples can be readily controlled through careful design of these components. In the present work, compression platens composed of a diamond crystal and a SiC fiber have been evaluated and compared. The diamond platen was prepared from a 1 mm long and 0.5 mm wide diamond crystal with a tapered end. The tip was prepared by mechanical grinding followed by FIB milling to produce a 40 µm x 40 µm flat surface perpendicular to the loading axis. A second tip was prepared from a SiC fiber, 8 mm in length by 0.1 mm in diameter, with the contact surface similarly shaped through FIB milling. The 80:1 aspect ratio of the SiC fiber platen yields a lateral stiffness that is quite low, measured to be less than 0.0001 N/µm. By comparison, the diamond platen exhibits a high lateral stiffness, measured to be 0.1 N/µm. The tensile grip was also fabricated from a SiC fiber and similarly exhibits a very low lateral stiffness. The shoulder-loading grip profile was machined into the fiber by FIB milling, as shown in Figure 1B.

A quasi-static testing methodology was employed to acquire images during these mechanical tests, where samples undergo sequential periods of loading, alternating with periods for image collection during which the actuator is held stationary. Images recorded in the present study had a size of 4096 x 2048 pixels for compression testing and 6000 x 2000 pixels for tension testing. This test control was automated using custom LabView scripts.

The material investigated here is the single crystal nickel-based superalloy René N5. This alloy is commonly used in turbine blade applications and is precipitation strengthened with a high volume fraction of coherent γ' precipitates (L1$_2$ crystal structure) in a solid solution γ matrix (FCC crystal structure). Despite a complex microstructure, a previous report on microcompression testing of this engineering alloy indicates a size-dependent response similar to pure metal FCC samples [12].

Microsamples were fabricated from the bulk substrate through a multi-step process described elsewhere [11] involving a combination of micro-EDM machining and FIB milling. The x-ray back-reflection Laue method was used to orient the samples to have a single-slip [$\bar{1}$23] loading direction with a [$\bar{1}$1$\bar{1}$] SEM viewing direction. The [$\bar{1}$1$\bar{1}$] viewing direction allows both the [$\bar{1}$23] loading direction and the [$\bar{1}$01] primary

slip direction to be contained within the imaging plane. A schematic model of a microcompression sample after slip has occurred on a single (111) primary slip plane is shown in Figure 2, indicating the important directions. The compression samples in this study were nominally 10 μm in diameter, with a 2.3:1 length to diameter aspect ratio. These were tested with both the high lateral stiffness diamond platen and the low lateral stiffness SiC fiber. The tensile specimens were nominally 11 μm in diameter with a gage length of approximately 55 μm, and were tested using the low lateral stiffness SiC fiber tensile grip shown in Figure 1B.

Due to the sample loading and viewing orientations employed here, it is possible to consider both axial and lateral displacements. Note that the lateral displacements are not evident in conventional stress-strain data. If the primary slip system accounts for all plastic flow, the displacement of the free end of the specimen relative to the fixed base will lie parallel to the primary slip direction $[\bar{1}01]$, as illustrated by the inset in Figure 2. Displacements were calculated from SEM images by tracking the motion of unique features that were machined into the sample surface via FIB milling. A custom LabView script was used to track the X and Y positions of these features within each image, corresponding to the axial ($\mathbf{d_A}$) and lateral ($\mathbf{d_L}$) displacements shown in the inset of Figure 2. Any displacement parallel to $[\bar{1}01]$ can be resolved into its orthogonal components, $\mathbf{d_A}$ and $\mathbf{d_L}$, where by geometry, $\mathbf{d_L}/\mathbf{d_A}$ =0.866 for a $[\bar{1}1\bar{1}]$ viewing orientation.

3. Micromechanical Test Results and 2D Displacement Measurements

Figure 3 shows a series of compression test flow curves, where constrained compression corresponds to tests conducted with the high lateral stiffness diamond platen and unconstrained compression corresponds to tests with the low lateral stiffness SiC fiber platen. The constrained compression experiments show a lower yield point and a smooth positive strain hardening regime. In contrast, the unconstrained tests exhibit higher yield points with periodic large strain bursts and overall negligible strain hardening. The strain bursts are accompanied by significant load drops followed by periods with rapid strain hardening rates (approaching the elastic modulus). The constrained compression yield stress measured at 1% engineering strain was about 1017 MPa, while that for the unconstrained compression was near 1083 MPa [11].

Careful examination of the images acquired during testing provides insight relating to dislocation activity. Figure 4A shows the image recorded at point "**i**" in the left inset of Figure 3, where it can be seen that a large strain burst occurred during image acquisition. The strain burst was captured within half a single raster line of the image, corresponding to an event duration of less than 30 ms. The stress value reported in the plot of Figure 3 was measured at the onset of image collection. Considering the geometrical illustration in Figure 2, the axial displacement is related to the shear displacement by $\mathbf{d_{101}}=(1.32)\mathbf{d_A}$. For an axial displacement of 820 nm, the shear displacement corresponds to approximately 4400 dislocations with a burgers vector of $a/2\,[\bar{1}01]$ propagating through the specimen in this initial strain burst.

Later during this same test, a second large strain burst occurs, terminating at "**ii**" in Figure 3. Figure 4B shows the image corresponding to this event, where it can be seen that slip occurred near the middle of the sample and is very localized. A thin band of

undisturbed surface topography extends from top to bottom of the microcrystal when a single slip system is active. This location marks the position about the circumference of the sample where the slip vector is tangent to the surface such that no slip step is produced on the sample surface. Note also that the slip steps on either side of the center band are accurately depicted in the geometric model in Figure 2. The overlay image in Figure 4C, again from "**ii**", illustrates highly local slip activation producing a sample with a uniformly sheared upper half and an unaffected lower half. The inset in 4C highlights an array of small pits that have been milled into the specimen surface using the FIB. The displacement along the diagonal line is parallel to $[\bar{1}01]$ and indicates the trace of the slip vector at the surface. Measurements were made for $\mathbf{d_A}$ and $\mathbf{d_L}$ from each of the three lines to give an average slip distance of 580 nm. This translates to a lower bound approximation of 2300 dislocations within a very narrow band of material, assuming dislocations have fully traversed the slip plane and are solely from the primary slip system. The experimentally measured ratio between lateral and axial displacements from this analysis gives $\mathbf{d_L} / \mathbf{d_A} = 0.84$, in good agreement with the predicted displacement ratio of 0.87.

The point in the constrained compression test labeled "**iii**" in Figure 3 corresponds to Figure 5A. Upon loading with the diamond platen beyond the elastic limit, a small number of individual slip bands appear on the surface of the deforming microsample. In Figure 5A, a set of four slip bands have formed as indicated by the arrows. At this point, all of the slip bands resulting from dislocation activity on primary (111) slip planes have been formed. In the remainder of the test, strain hardening progresses in part, through growth of these preexisting bands as evidenced by broadening of these same four bands as shown in Figure 5B. Figure 5C shows an overlay of the images recorded before and after a small strain burst. When compared with Figure 4C, clear distinctions can be made between strain bursts occurring in laterally constrained and unconstrained compression tests. As noted in our earlier work [11], constrained experiments require activation of the secondary $(\bar{1}\bar{1}1)[011]$ slip system to accommodate lateral offsets resulting from slip activity on the primary system. Under constrained compression, the net strain is nearly axial and more uniformly distributed over the sample volume.

Figure 3 also contains stress-strain curves from micro-scale tension experiments conducted using a laterally compliant SiC fiber tensile grip. Two immediate observations are clear from this data. The yield stresses for the tension tests are higher than that for any of the compression tests, while the plastic flow stresses are much lower. Large strain bursts are evident in one tension curve, while the other two exhibit limited events of such magnitude. The tension inset in Figure 3 highlights two of these tests, from which images have been selected for closer examination.

The microtension sample presented in Figure 6 corresponds to the highly serrated flow curve in Figure 3, with corresponding points "**a**", "**b**" and "**c**". The image recorded at "**a**" shows a single slip band associated with the initial yielding of this microsample. The band has a width of 2-3 microns, with a gradual transition from slipped to unslipped material. The second, larger strain burst, that follows introduces multiple slip bands into the gage of the sample immediately next to the initial slip location. These slip steps are much more localized. Finally, near the end of the test at "**c**", after six distinct bursts, additional slip steps have propagated from the initial band and always display localized glide along a sharp disruption. A similar slip morphology can be seen in the

unconstrained compression test specimens with respect to the discrete steps formed during flow of these microcrystals.

The second curve from the tension inset of Figure 3 contains points "**d**" and "**e**". It is also characterized by a massive strain burst at yielding, but then subsequent plastic flow is not serrated. The specimen morphologies associated with "**d**" and "**e**" are shown in Figure 7. The inset of Figure 7 identifies the general location where slip occurred during the initial strain burst. An individual carbide particle, indicated by the arrow, is evidence that the microcrystal was likely extracted from an interdendritic region within the microstructure. The interdendritic regions of cast engineering alloys such as René N5 are known to contain heterogeneities, including pores and carbides, on the scale of these specimen dimensions, which can influence the flow behavior [12].

Figure 8 shows results of digital image analysis used to track movement of the free end of each microcrystal for the two modes of in-situ compression testing. This plot presents displacements of the top of each sample relative to its base along the orthogonal directions of interest, d_A and d_L. Unconstrained SiC tests follow a linear trend that is controlled by geometrical influences alone. The slope of the unconstrained test data is about 0.92, quite close to the pure geometric displacement ratio of $d_L/d_A = 0.866$ for $[\bar{1}01]$ single-slip when viewed from the $[\bar{1}1\bar{1}]$ direction. In contrast, laterally constrained compression samples display a limited amount of lateral displacement. In these experiments, lateral sample displacements resulting from activity on the primary slip system are inhibited by the resistance to lateral movement of the diamond platen. The inset plot of Figure 8 shows the lateral force acting on the deforming samples as a result of the lateral stiffness in the diamond platen (0.1 N/µm). As a result, during loading as deformation transitions from elastic to plastic, activity on the primary slip system must be accompanied by secondary slip to produce the net purely axial strain observed in Figure 5. Although not shown in Figure 8, the ends of specimens under tensile loading with laterally compliant grips show dramatic initial lateral displacements associated with large strain bursts at yielding. Subsequent deformation leads to the realignment of the tensile grip along the loading axis, as the bending forces act perpendicular to the applied load [13].

4. Summary

In unconstrained microcompression experiments, where the lateral stiffness of the test frame is practically negligible, the contact end of a microcrystal is free to move during deformation. The deformed sample morphology matched the expected shape change for single-slip deformation, including the ratio of measured lateral and axial displacements. Individual tests show variation in yield point, which is likely related to the distribution of available dislocation nucleation sources within each specimen.

In constrained compression experiments, a restoring force acts in opposition to lateral displacements. The morphology of deforming microcrystals shows barreling and the lateral displacement at the contact end of the specimen is limited. This results from the high lateral stiffness of the diamond tip, 0.1 N/µm. Thus, displacements are almost purely axial for the example in Figure 5C, where the developed lateral force reaches 0.016 N when the applied axial force is 0.085 N. This lateral restoring force is significant, with the stiff compression platen activating secondary slip at the onset of

plasticity. In-situ imaging throughout the test suggests that this secondary activity is quite uniform across the specimens.

Compression tests often suffer from the intrinsic loading artifact of stress concentrations at the platen contact. These become more pronounced for increasingly smaller specimen dimensions due to sample preparation challenges. Tension tests provide a more uniform state of stress within the gage length. The present tension experiments show higher yield points, which are likely related to this stress uniformity. Flow stress levels in these tension tests are below that for compression tests and are a topic of ongoing study.

The micromechanical behavior of the single crystal nickel-base superalloy René N5, tested under three distinct conditions, displays three distinct flow curves. In-situ testing within the SEM has provided qualitative imaging of deformation morphology to describe slip activity. Quantitative characterization of microcrystal displacements was also used to describe shape change in 3D. Specific boundary conditions in the compression and tension experiments determine the flow behavior, affecting both stress-strain properties and deformation morphology. With no lateral constraints, deformation is defined entirely by the crystallography of the specimen under loading. In contrast, highly constrained tests experience an additional lateral force that develops with deformation, encouraging secondary slip system activity. Quantitative visualization of specimen morphology during testing is an invaluable tool to interpreting the deformation behavior.

References

[1]   M.D. Uchic, D.M. Dimiduk, J. Florando, W.D. Nix, Science 305 (2004) 986-989.
[2]   D.S. Gionola and C. Eberl, JOM 61(3), (2009) 24-35.
[3]   M.D. Uchic, P.A. Shade and D.M. Dimiduk, Annu. Rev. Mater. Res. 39 (2009) 361-386.
[4]   G. Dehm, Prog. Mater. Sci. 54 (2009) 664-88.
[5]   O. Kraft, P.A. Gruber, R. Monig and D. Weygand, Annu. Rev. Mater. Res. 40 (2010) 293-317
[6]   M. Legros, D.S. Gianola and C. Motz, MRS Bulletin 35 (2010) 354-360.
[7]   J.R. Greer, J.T. De Hosson, Prog. Mater. Sci. 56 (2011) 654-724.
[8]   M.D. Uchic, D.M. Dimiduk, R. Wheeler, P.A. Shade, H.L. Fraser, Scripta Mater. 54 (2006) 759-764.
[9]   D. Kiener, W. Grosinger, G. Dehm, Scripta Mater. 60 (2009) 148-51.
[10]   D. Kiener, C. Motz, G. Dehm, Mater. Sci. Eng. A 505 (2009) 79-87.
[11]   P.A. Shade, R. Wheeler, Y.S. Choi, M.D. Uchic, D.M. Dimiduk, H.L. Fraser, Acta Materialia 57 (2009) 4580-87.
[12]   P.A. Shade, M.D. Uchic, D.M. Dimiduk, G.B. Viswanathan, R. Wheeler, H.L. Fraser, Mater. Sci. Eng. A, In Press.
[13]   G.I. Taylor, W.S. Farren, Proc. Roy. Soc. A 111 (1926) 529-551.

Figure Captions

Figure 1. (A) Device for conducting in-situ micro-scale mechanical tests in an SEM [11]. (B) Tensile grip shown approaching a tension specimen attached to the bulk substrate.

Figure 2. Schematic representation of a microcompression sample showing the loading direction [$\bar{1}23$], primary slip direction [$\bar{1}01$], and primary slip plane (111), relative to the [$\bar{1}1\bar{1}$] viewing direction. The inset shows sample displacement resolved into axial displacement, $\mathbf{d_A}$, and lateral displacement, $\mathbf{d_L}$.

Figure 3. Stress-strain curves for in-situ mechanical tests on Rene N5 microcrystals. Compression tests conducted on 10 μm diameter samples are shown by open data points and tension tests on 11 μm diameter samples by solid data points. Key features of the flow curves are labeled for reference in the text.

Figure 4. SEM images acquired at various points in time during an unconstrained compression test in Figure 3. (A) Image recorded at "**i**", as yielding occurred during hold stage showing rapid strain burst, (B) Image corresponding to "**ii**" in flow curve, (C) Overlay image of B with preceding image. Inset shows axial and lateral displacements, $\mathbf{d_A}$ and $\mathbf{d_L}$, from B.

Figure 5. SEM images showing four distinct slip bands formed in the constrained compression test shown in Figure 3. (A) At the point labeled "**iii**", the last slip band has formed and strain hardening begins. (B) At "**iv**", the existing bands formed at "**iii**" have broadened. (C) An overlay of the images bounding "**iv**" highlights the lack of lateral displacement as compared to Figure 4.

Figure 6. SEM images recorded from tension tests, with images corresponding to points "**a**", "**b**" and "**c**" of Figure 3. Note the well-defined slip steps for the test exhibiting the serrated appearance.

Figure 7. Tension test images taken from the sample whose stress-strain curve contains points "**d**" and "**e**" in Figure 3. The inset shows a carbide inclusion in the region where deformation first initiated.

Figure 8. Axial and lateral displacements of the upper, free end of the microsamples, measured relative to the fixed base during compression tests carried out with the low lateral stiffness SiC fiber platen and the high lateral stiffness diamond platen. The inset shows the lateral force exerted by the diamond at the platen contact due to dislocation motion on the primary slip system.
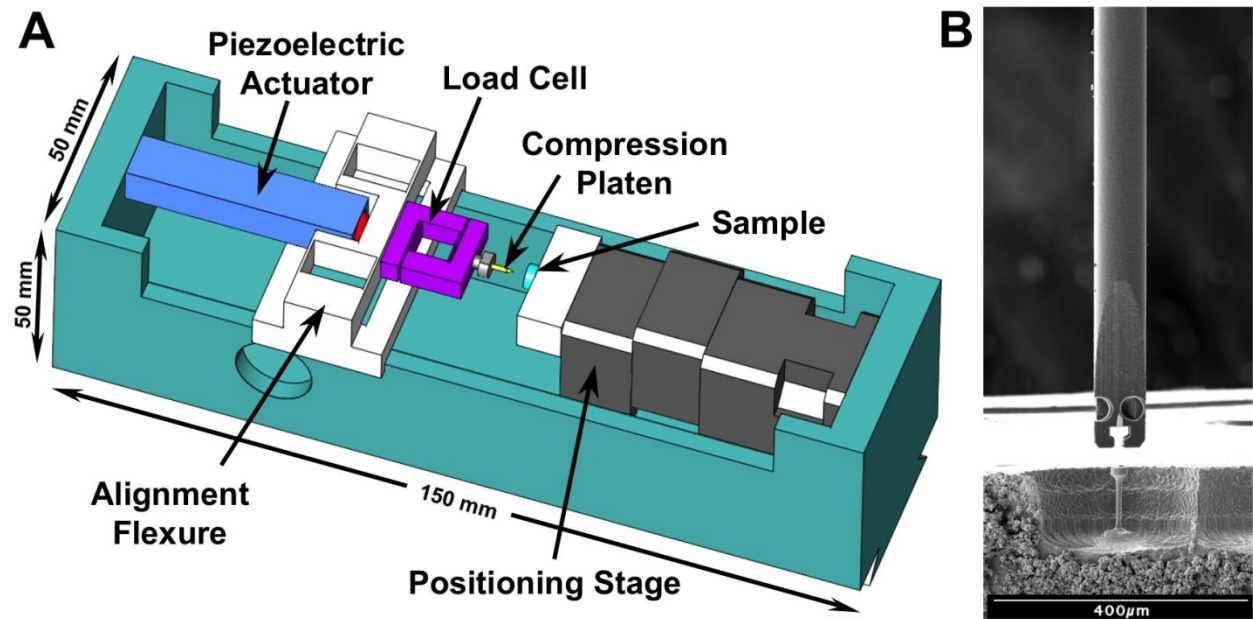
Figure 1. (A) Device for conducting in-situ micro-scale mechanical tests in an SEM [11].
(B) Tensile grip shown approaching a tension specimen attached to the bulk
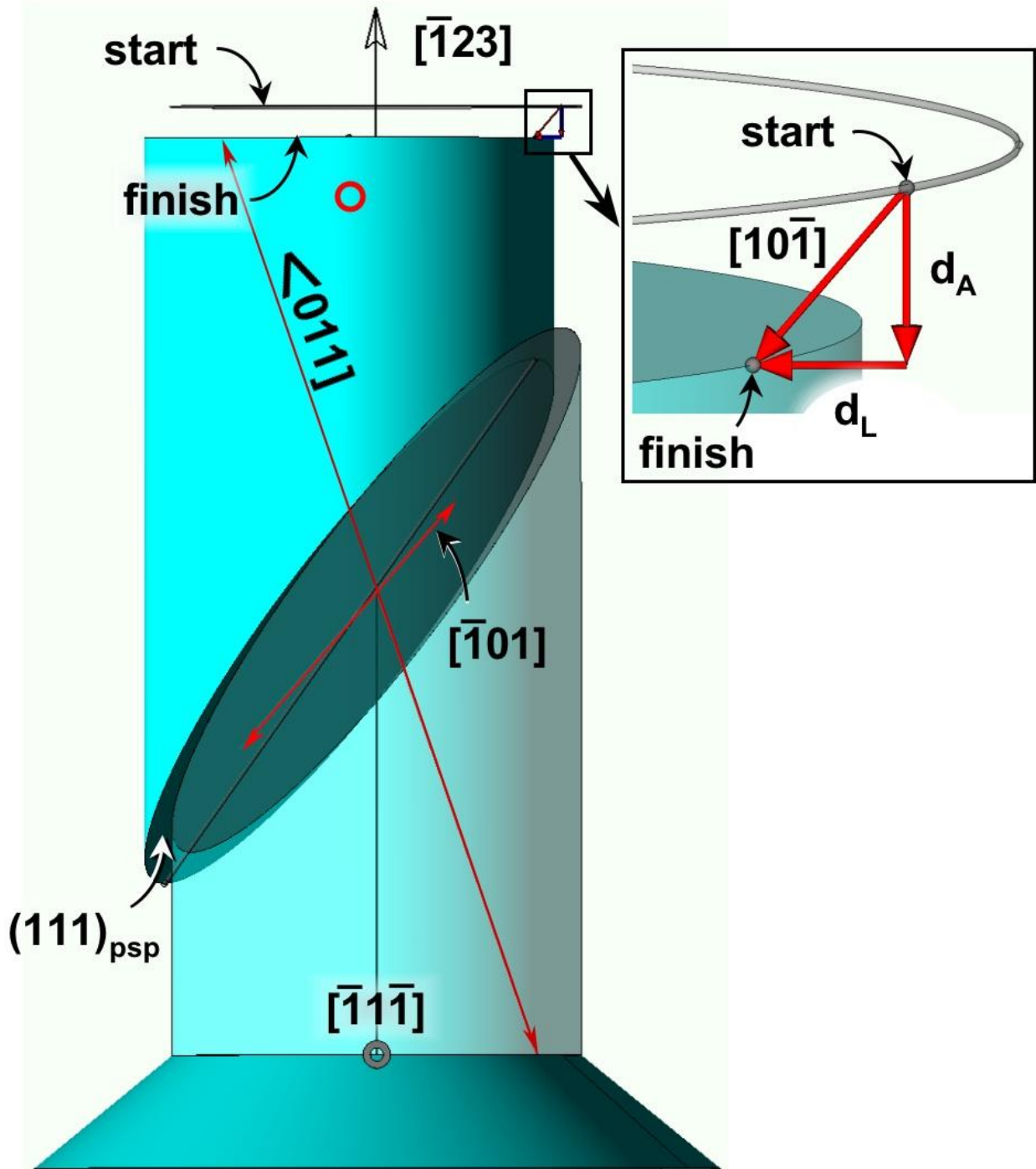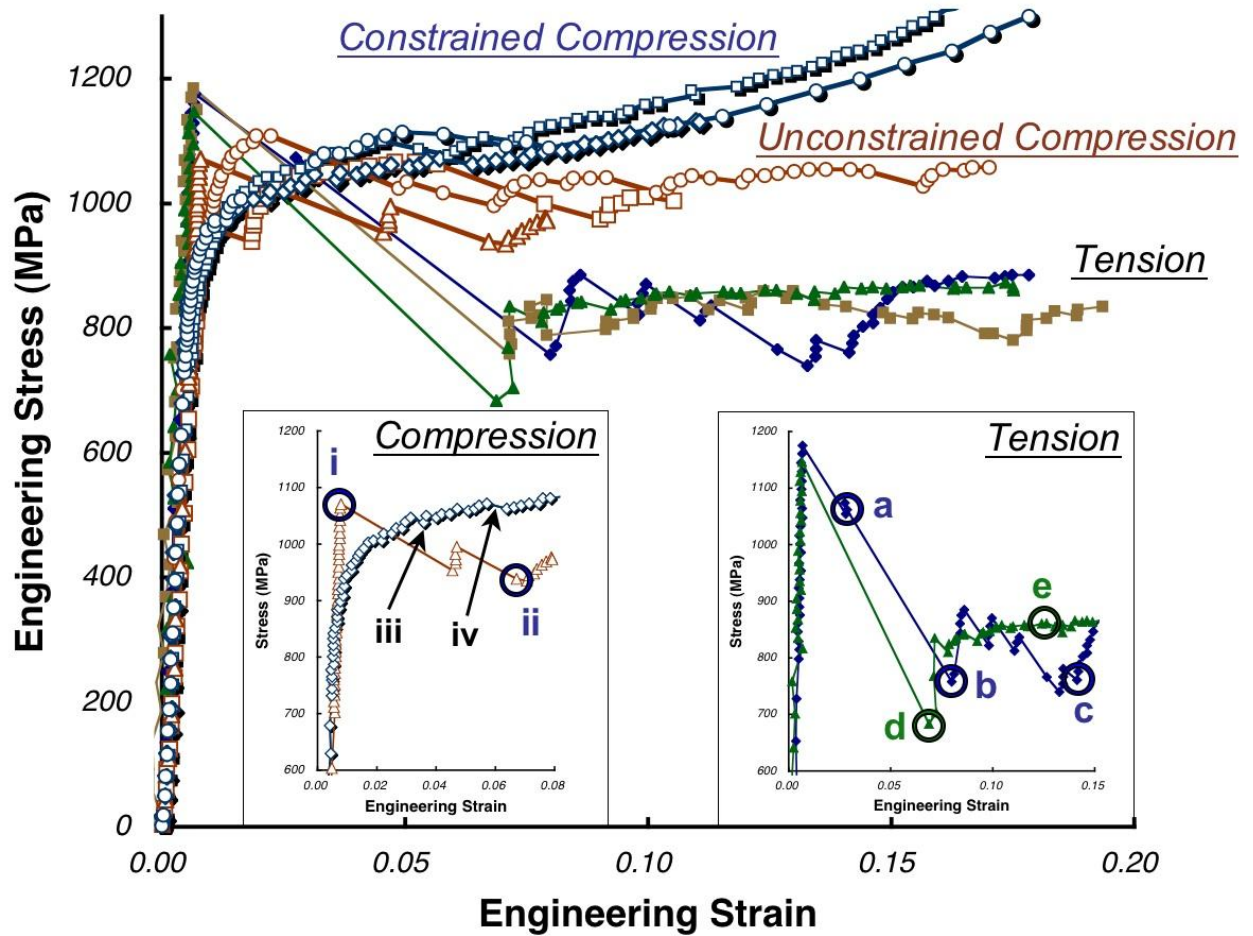substrate.

Figure 2. Schematic representation of a microcompression sample showing the loading direction [$\bar{1}23$], primary slip direction [$\bar{1}01$], and primary slip plane (111), relative to the [$\bar{1}1\bar{1}$] viewing direction. The inset shows sample displacement resolved into axial displacement, $\mathbf{d_A}$, and lateral displacement, $\mathbf{d_L}$.

Figure 3. Stress-strain curves for in-situ mechanical tests on Rene N5 microcrystals. Compression tests conducted on 10 µm diameter samples are shown by open data points and tension tests on 11 µm diameter samples by solid data points. Key features of the flow curves are labeled for reference in the text.
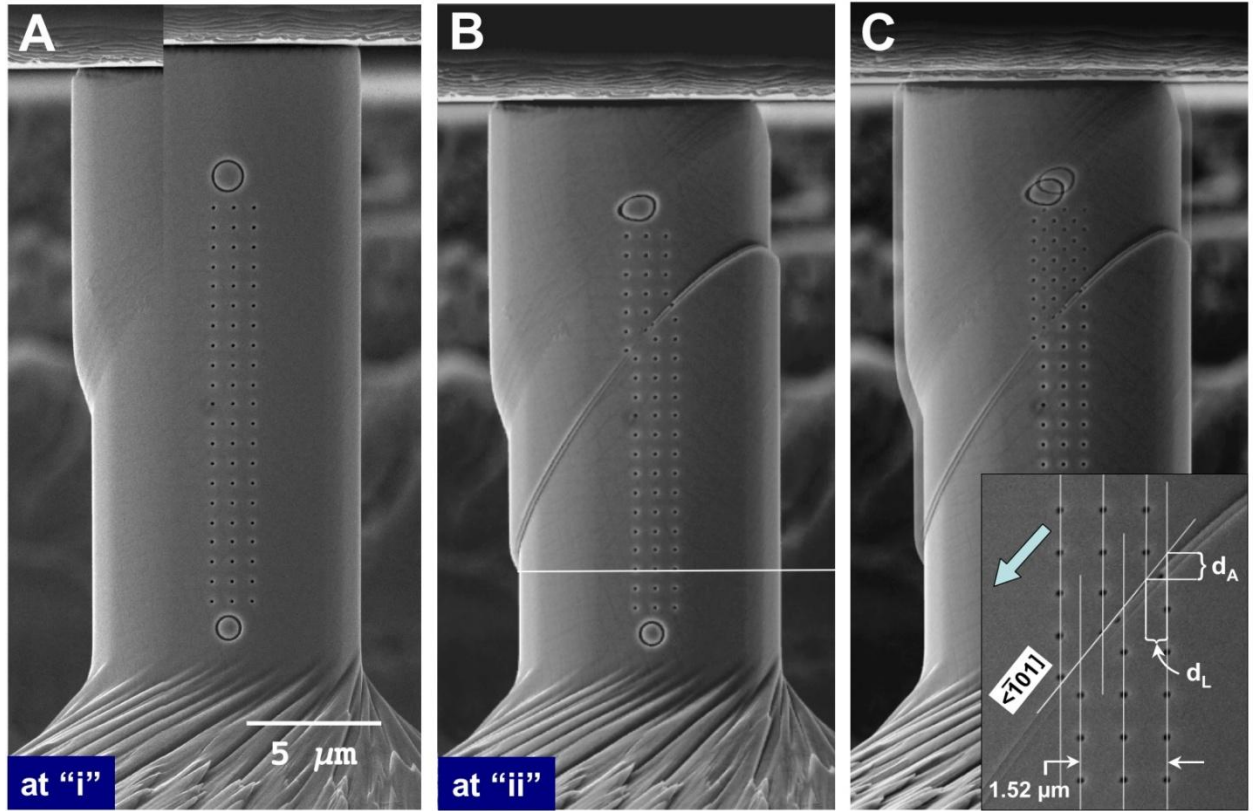
Figure 4. SEM images acquired at various points in time during an unconstrained compression test in Figure 3. (A) Image recorded at "**i**", as yielding occurred during hold stage showing rapid strain burst, (B) Image corresponding to "**ii**" in flow curve, (C) Overlay image of B with preceding image. Inset shows axial and lateral displacements, $\mathbf{d_A}$ and $\mathbf{d_L}$, from B.
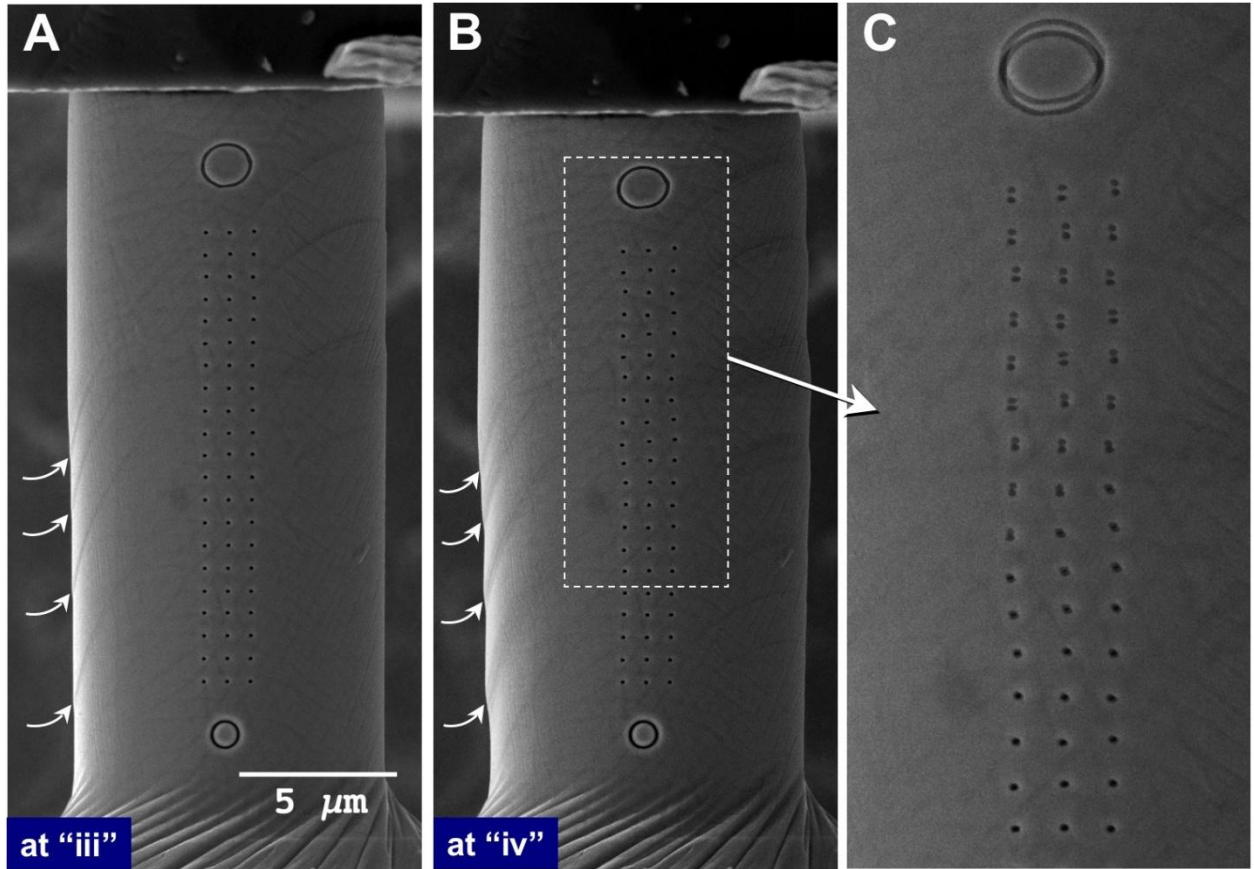
Figure 5. SEM images showing four distinct slip bands formed in the constrained compression test shown in Figure 3. (A) At the point labeled "**iii**", the last slip band has formed and strain hardening begins. (B) At "**iv**", the existing bands formed at "**iii**" have broadened. (C) An overlay of the images bounding "**iv**" highlights the lack of lateral displacement as compared to Figure 4.
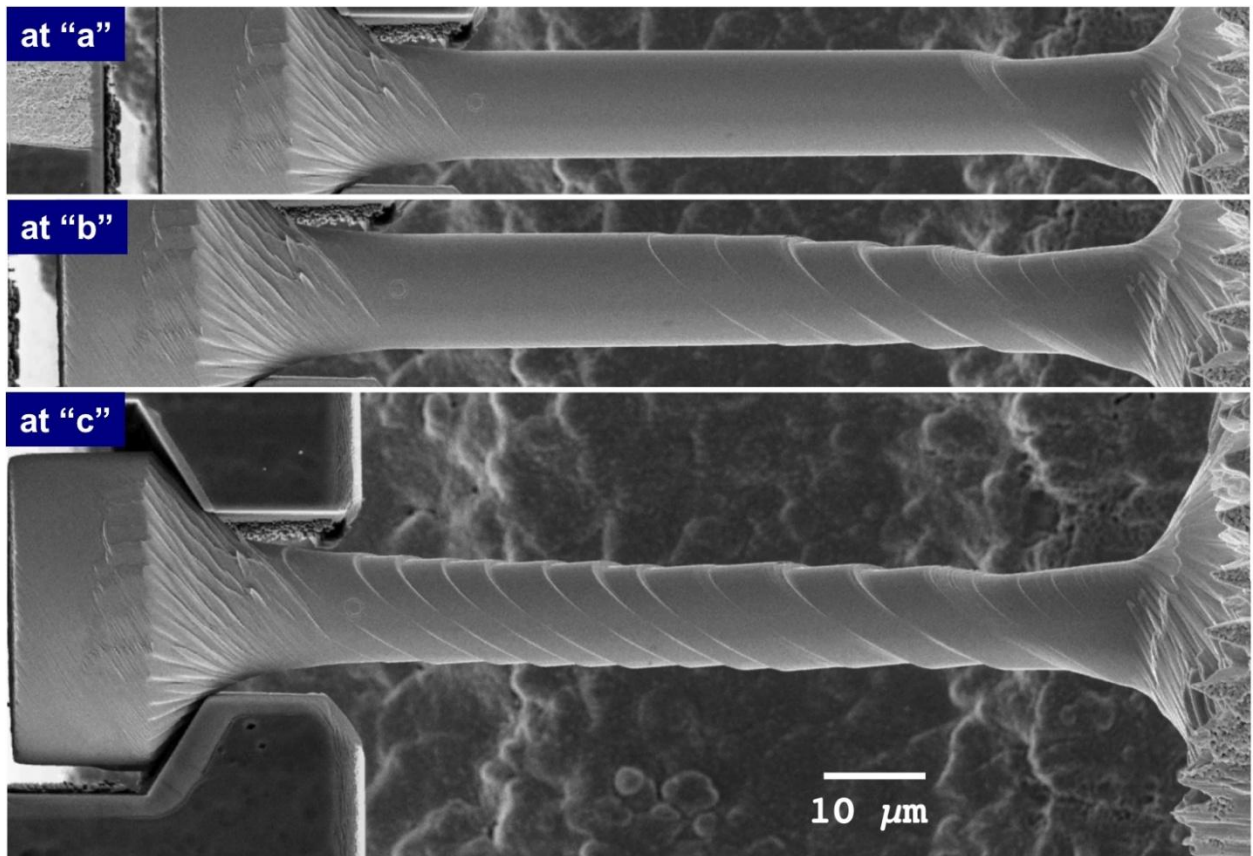
Figure 6. SEM images recorded from tension tests, with images corresponding to points "**a**", "**b**" and "**c**" of Figure 3. Note the well-defined slip steps for the test exhibiting the serrated appearance.
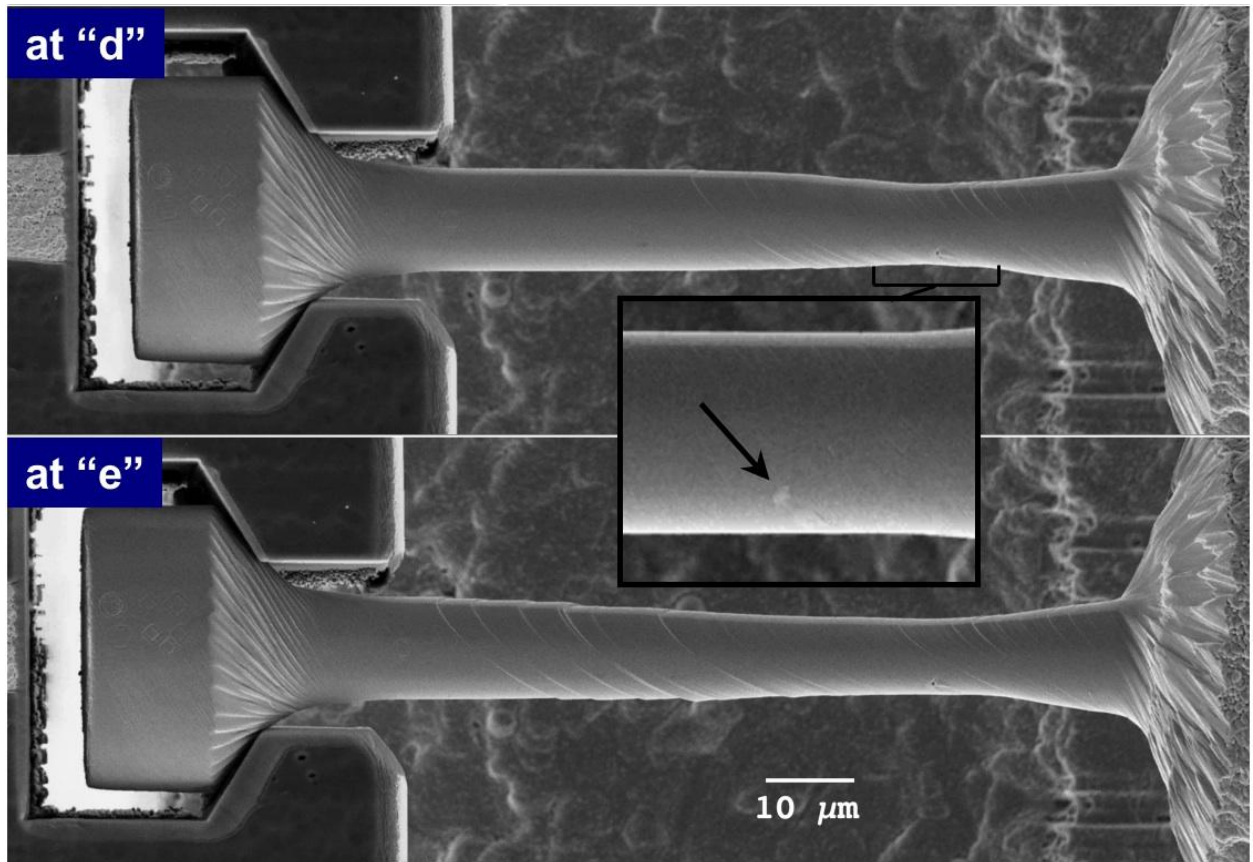
Figure 7. Tension test images taken from the sample whose stress-strain curve contains points "**d**" and "**e**" in Figure 3. The inset shows a carbide inclusion in the region where deformation first initiated.
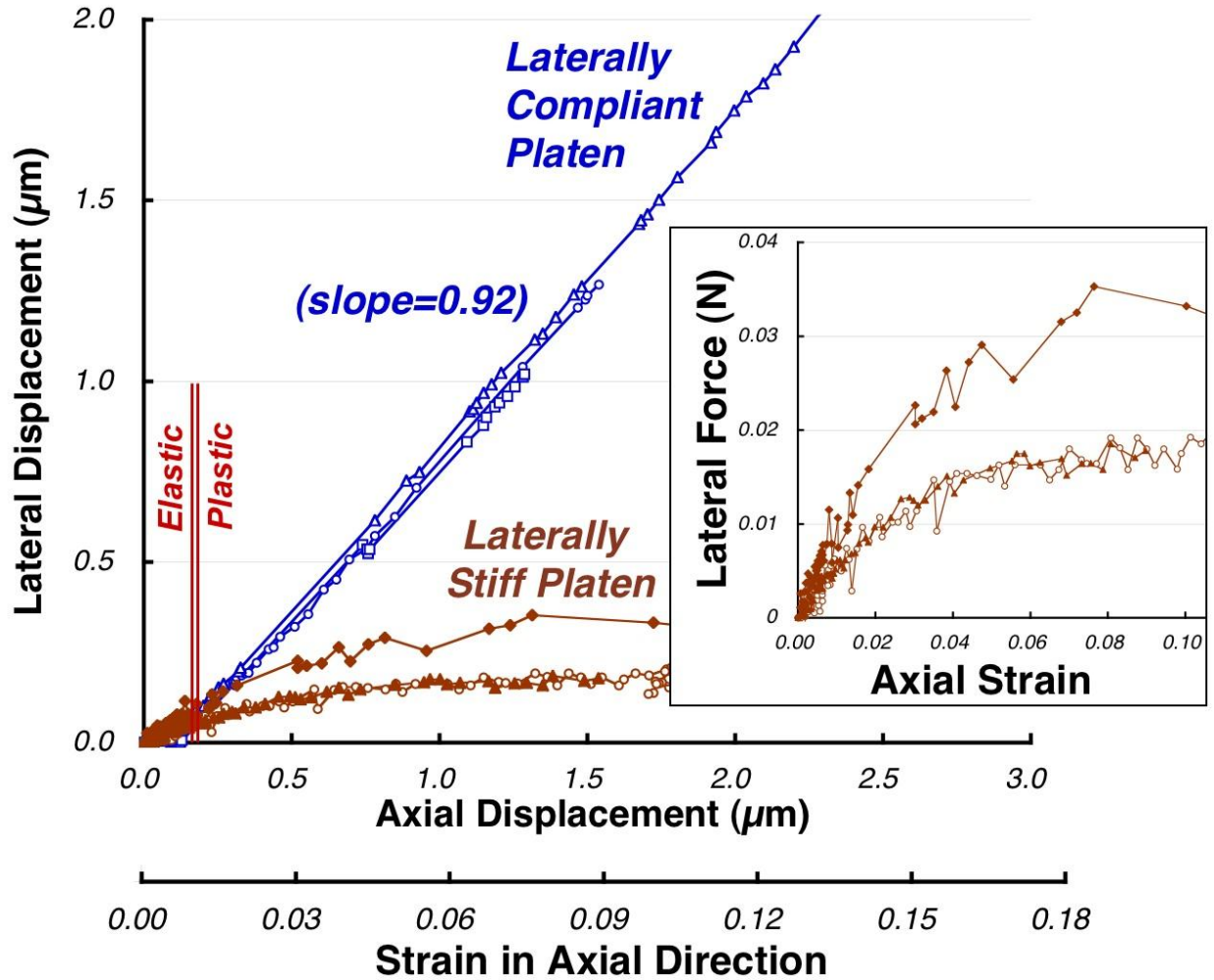
Figure 8. Axial and lateral displacements of the upper, free end of the microsamples, measured relative to the fixed base during compression tests carried out with the low lateral stiffness SiC fiber platen and the high lateral stiffness diamond platen. The inset shows the lateral force exerted by the diamond at the platen contact due to dislocation motion on the primary slip system.